International Journal of Computing and Digital Systems
ISSN (2210-142X)
Int. J. Com. Dig. Sys. 9, No.4 (July-2020)

http://dx.doi.org/10.12785/ijcds/090401

CHIMES: Chemical Identification By Magneto Elastic Sensing

Yeshak Dabels[1], Yasser Ismail[1] and Fred Lacy[1]

[1]Electrical Engineering Department, College of Sciences and Engineering, Southern University and A&M College, Baton Rouge, LA, USA

Received 31 Dec. 2019, Revised 17 Mar. 2020, Accepted 23 Jun. 2020, Published 1 Jul. 2020

Abstract: A Chemical Identification by Magnetoelastic Sensing (ChIMES) technology is hereby presented in this paper. The sensor is designed to detect and identify a broad range of gaseous analytes using a single or array of sensors located in a flow tube. The sensor is capable of untethered communication through the metallic or the nonmetallic barrier. This gives the sensor a unique feature that provides many capabilities for interrogation where the proliferation of the sample environment is not possible due to health, safety, legal, or environmental concerns. As the analyte flows through a tube containing a sensor array (sensors constructed of an amorphous wire sensing element and a target response material (TRM)), the TRM absorbs the analyte which will typically swell imposing stress on the amorphous wire embedded in the core of the sensor. As the TRM applies pressure to the amorphous wire, the wire's magnetic permeability changes, which is sensed by the ChIMES system instrumentation. Since each sensor in the array is designed to respond differently to various analytes, the specific analyte and its concentration can be determined by analyzing the rise time, fall time and amplitudes of the various sensors. The size of this electronics package is greatly reduced so that a handheld version of the ChIMES system could be constructed. The device total weight is estimated to be approximately 6 to 10 Pounds with the overall volume of 150 〖In〗^3. The battery life is expected to last 4 hrs with a duty cycle of 0.25 %.

Keywords: Media Magnetoelastic sensing, Target response material, Sensy wire, AC drive coil, Cancellation coil, Duty cycle

1. INTRODUCTION

The demand for more and better sensors due to increased use and dependence has prompted more advances in material science, photonics and microelectromechanical systems. These advances have led to the development of many innovative chemical sensors, with principles of detection based on quartz-crystal microbalances, surface acoustic waves, microcantilever, flexural plate, and various optical absorbance and fluorescence techniques [1], [2]. About all these sensors, like their predecessors operate under the same basic principles of the mechanical or the electrical connection between the sensing element and the control and reporting component of the device. Therefore, interrogation of materials where penetration is restricted due to health hazards, safety, or environmental concerns with such sensors is unsuitable.

Among various sensors technologies, gas sensor technology is used across a wide variety of targets and can interrogate through both metallic and nonmetallic barriers. Chemical Identification by Magneto-Elastic Sensing (ChIMES), shown in Figure 1, relies on the change in the magnetic permeability of an amorphous magnetoelastic wire due to induced stress on the wire [3], [4]. As a "target response material" (TRM), which is tailored, to respond to specific gas molecules respond by swelling, it imposes stress on the magnetoelastic (SENCY) wire embedded along with its axial core as shown in Figure 2 [4]. Many sensor technologies have now been based on magnetoelastic materials. Grimes [11] developed many sensors in which the principle of detection relies on changes in the resonant frequency of an amorphous ferromagnetic foil coated with a material responsive to a specific chemical or biological analytes. ChIMES uses this principle to read and display the changes in the resonant frequency of an amorphous ferromagnetic sensor.

E-mail: yeshakdabels@gmail.com, yasser_ismail@subr.edu, fred_lacy@subr.edu

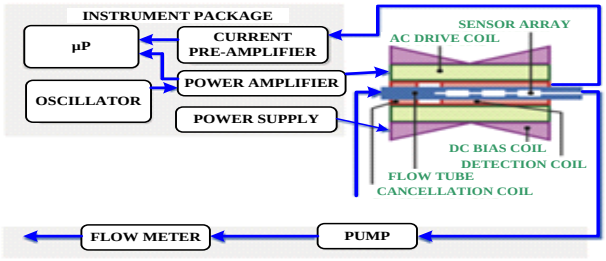

Figure 1. ChIMES Sensor Block Diagram [4], [5].

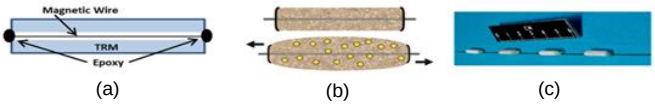

Figure 2. (A) Schematic of ChIMES sensor; (b) Exposure to analyte causes the TRM to swell, imposing axial stress on the magnetoelastic wire; and (c) Photograph of four sensors mounted on a stiff fiber.

Upon the mass change of chemically responsive layers, magnetoelastic sensors have been used to monitor CO2, NH3, pH, and glucose-based [11]. an excitation coil is used to induce a magnetic field on the sensor while the detection/cancellation coil set is remotely used to observe the change in permeability of the SENCY wire as the magnetic domains in the wire switches. The ChIMES instrumentation is used to measure changes in the Faraday voltage as a function of stress [4]. After the wire has been extended due to the induced stress by 0.1% in the axial direction a measurable change in the wire permeability is possible as shown in Figure 3 [3], [4].

The paper is organized as follows. Section 2 presents the problem formulation and the motivation of this work. Insights on the types of sensors are discussed in section 3. Section 4 provides the theoretical background of the handheld ChIMES instrumentation and the design process; this work will focus only on parts of the instrumentation and will not deal with the microprocessor, or the sensor element. Section 5 presents the results of our finding and their implications which are the benchmark for the identification of chemicals by a handheld ChIMES. Finally, conclusion and future work are drawn.

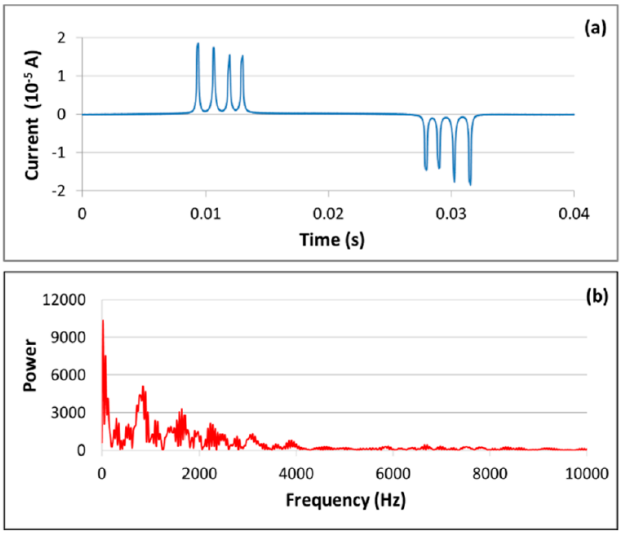

Figure 3. (a) Magnetic switching domain signals obtained from a linear array of four sensors; and (b) Frequency content of part **a** using a 100-μm-diameter SENCY wire [7].

2. PROBLEM FORMULATION AND MOTIVATION OF THIS WORK

The ChIMES instrumentation sensor is currently a benchtop device that has almost the same size of carry-on luggage. Because of this, the system cannot be moved around easily to perform applications such as passive gamma detection as in areas intended to perform, so analytes will have to be transported to a station that housed the sensor. This process of transporting analytes defeats the major purpose of the design of the device which operates with an untethered communication between the sensor and the device electronics, this design was made to operate without disturbing the environment in which was under investigation. To use the ChIMES sensor to its full capability, it is eminent to research and miniaturize a handheld version of the device for easy portability due to the aforementioned shortcomings of the benchtop version. This will enable the operation of the device in all conditions and locations successfully without disturbing the scene of the analyte when necessary.

The ChIMES system has a wide range of application capabilities including industry, hospitals and other institutions. But this capability becomes limited due to size, weight and supply power. To use this system to its full potential, the system needs to undergo a tremendous strip-down of weight and size. The issue of weight and size is important in terms of transporting of the device to remote areas for use, therefore a reduction in size and weight will greatly improve the service range of the device in remote locations and small confined locations as well.

The use of an ac power source from a wall outlet or generators is a drawback for portable devices. Because this system intends to have the ability to reach and interrogate gases without disturbing the source due to

safety, health or environmental considerations, designing the ChiMES as a handheld portable device to run on a 12V rechargeable battery is the best way of allowing the system to reach its potentials. Miniaturizing the ChIMES to a handheld version gives users the ability to use the system to its full potential.

3. MAGNETO-IMPEDANCE SENSORS DESIGN

Sensors are devices used to measure properties, such as temperature, position, pressure, or acceleration, and respond with feedback through the responding material, then interpreted by the instrumentation package. In this section, we will review extensively the design of magneto-impedance sensors. Because there is no technology that is closely similar to the ChIMES technology, we will also show briefly the design and implementation of a GMI sensor which could be considered as one of the current technologies that are designed on the same general idea to that of the ChIMES but yet very different in several ways.

A. Circuit Designing of Bio-Magnetic Sensor using Giant Magneto-Impedance Effect

The detection of bio-magnetic activities through a non-invasive and non-contact evaluation of electrical activity in living organisms was demonstrated and published by Nilma in 2017 in an international journal of engineering research and reviews. The paper showed how to achieve bio-magnetic field detection in a non-magnetically shielded environment based on the principle of the Giant Magneto-Impedance (GMI) effect in amorphous wire and carried out experiments to obtain the circuit design requirements.

Extremely weak magnetic fields are only detectable with exquisitely sensitive equipment that can block out all external magnetic fields. It requires a superconducting quantum interference device (SQUID) with sensitivity at the Femto-Tesla (fT) in a magnetically shielded room (MSR) to detect these extremely weak fields [2], [6-8]. Because this technology requires special equipment such as a magnetic shield room and other larger devices possibly a cooling container, the SQUID system becomes too cumbersome and expensive for personal and laboratory use [2], [6-8].

Because very weak magnetic fields require an extremely sensitive micro-magnetic sensor to detect biomagnetic fields. In 1993, Professor K. Mohri found a new electromagnetic phenomenon in the amorphous wire and named it as GMI effect, in which the impedance of the amorphous wire sensitivity changed with a small external applied magnetic field when a high-frequency current was applied through the wire as a carrier [4], [3], [9]. Based on the GMI effect, they have developed sensitive micro magnetic sensors, called “MI sensor”, with the sensitivity of 1pT level [9], and also realized the bio-magnetic field detection in a non-magnetically shielded environment at room temperature [4], [3], [9]. In comparison with conventional magnetic sensors [Hall sensor, magnetoresistive (MR) sensor, and giant magnetoresistive (GMR) sensor] the MI sensor has an advantageous feature of high sensitivity. Table I illustrates the configuration of the magnetic sensor utilizing amorphous wire [4], [3], [9].

TABLE I. COMPARISON OF MAGNETIC SENSORS [1].

Sensor	Head length (3m)	Resolution (10^{-4}T)	Response Speed	Power consumption
Hall sensor	10-100	0.5/±1K	1 MHz	10 mW
MR sensor	10-100	0.1/±100	1 MHz	10 mW
GMR sensor	10-100	0.01/±20	1 MHz	10 mW
Fluxgate	10-20	13/±3	5 MHz	1 W
MI sensor	1K-2K	13/±3	1 MHz	10 mW

B. Circuit Design Requirement

The background uniform noise is canceled by the GMI gradiometer to ensure the detection of very weak magnetic fields. The sensor head in this application is constructed from amorphous Co-Fe-Si-B (constructed by Ningbo Institute of Industrial Technology, CAS) wire and has two coils: Sensing coil and a reference coil [10], [11]. The coil sets are separated by a distance of 3.5cm. The sharp pulse current which has a 20% duty cycle and a frequency of 2MHz feeds the amorphous wire through a 500 turn coil is wound around the amorphous wire is used to pick up the voltage reflecting external magnetic field variation [10], [11].

GMI Head Circuit

The sharp pulse current generator circuit is designed with adjustable pulse width and frequency to compensate for the amorphous wire's poor consistency. Since different parts of the wire have a different optimum working point. A Hex inverter is used to apply the 2MHz current pulse generated by the square-wave voltage generator to the amorphous wire as a carrier. This is done after the differential circuits transfer the square wave into a positive sharp pulse [10], [11].

Amplifier and Filter Circuit

Since detected magnetic fields are weak, a high gain (A>=100,000) amplifier is required [10], [11]. This produces a reasonable signal for further processing. Different orders of amplifiers are suggested to achieve this and obtain a stable circuit. The Amplifier circuit saturation is prevented by incorporating several low cut and high cut electric filters which eliminate power frequency interference and filter out DC components.

This is achieved by designing an AC coupled circuit (0.5Hz High pass filter) to eliminate the DC component intended to PREVENT next order circuit saturation [10], [11].

4. CHIMES INSTRUMENTATION SYSTEM DESIGN AND COMPONENTS

The ChIMES instrumentation system is made up of different individual components that are working in tandem as seen in Figure 4. This work will cover the complete design and implementation of the following major components: (i) the power supply; (ii) duplicate power amplifier; (iii) current pre-amplifier; (iv) AC drive coil; (v) detection/cancellation coil; and (vi) DC bias coil; (vii) Screen and microprocessor; (viii) pump/ flow meter. These components are addressed in this section and individually designed, tested and connected in tandem to operate as a single unit. The design process of each component is described below.

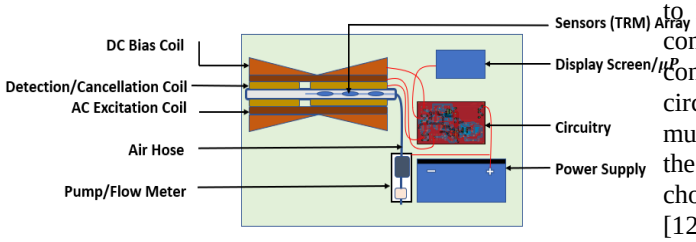

Figure 4. ChIMES instrumentation system.

A. The Power Supply

The entire system is powered by a LiFePO4 LF-LA12V9 battery which has a 12V 9Ah, 108Wh, 18A rating (Figure 5). This battery has dimensions of 5.95 X 2.6 X 3.76 inches and weighs 2lb 9oz [12]. The selected battery pack will help conserve weight without significant loss of power.

Figure 5. The 12V LiFePO4 battery.

The major component of the system runs on a 15V power supply, however, a 12V battery supply is the preferred choice because of several reasons.

The system is designed with the user in mind since the device will be a handheld portable device, a 12V battery pack becomes an easier choice over the 15V due to the availability of 12V supply in vehicles. Li-ion battery is considered one of the very few best batteries because the batteries are lightweight and have the highest energy density (mAh/weight). A DC to DC converter will be used to provide the proper voltage needed by the circuitry from a single battery.

B. The Circuitry

The PCB consist of the following devices: DC-DC Converter; the oscillator; AC and DC power supply; low noise transimpedance amplifier; ac drive (excitation) coil; dc bias coil which will all be discussed in below.

C. DC-DC Converter

There are several types of converters available for different applications. The TRC TEN 60-1223 ±15V DC to DC boost converter Figure 6 converts the 12V supply to 15V output with sufficient current. When choosing a converter, voltage level alone is not sufficient. The converter has to be able to deliver enough power to the circuit, this power factor is a function of voltage multiplied by the current which must be at least equal to the power consumed by the circuit. The converter of choice has 90% efficiency and provides 60W of power [12]. This device is one of a few available converters that is fairly small yet still able to provide ample power to the circuit. The efficiency of the converter is greatly important. Because the inefficiency will become a liability to the battery during conversion, and no converter is 100 percent, the efficiency of the converter is subtracted from 100% and the difference is considered a load to the battery as shown below.

Figure 6. The TRC TEN 60-1223 ±15V DC to DC boost converter.

From the given power analysis in Table II, the efficiency of the converter is given as Efficiency = $\frac{P_{OUT}}{P_{IN}}$ ×100 %. Therefore, this equation can be used to determine the input power (and current) the convert will require to deliver the 15V and -15V required output voltages for both rails.

TABLE II. POWER *ANALYSIS TABLE*.

Item No.	Device Name	Pos. 12 V Supply	Neg. 12V Supply	Pos. 5 V Supply	Power Consumed/Device (W)	Battery Supply
1	Low Noise Pre Amp	0.018	0.018		0.432	
2	Oscillator	0.001	0.001		0.024	
3	AC Power Amp	0.334	0.332		7.992	
4	DC Power Amp	0.337	0.336			
5	Air Pump	1.2			14.4	
6	Microprocessor			2.5	12.5	
7	Display Screen			2	10	
8	LabJack T7				0	
9	DC/DC Converter Inefficiency	0.21	0.11	0.21	1.05	
10	Battery Supply (Ah)					9
	Total Current (A)	**2.1**	**0.797**	**4.71**		**18 (Amp Rate)**
	Total Power (W)	**25.2**	**9.564**	**23.55**	**46.398**	

Assume:

P_{IN} = Converter input supply from the battery; $+P_{OUT}$ = Converter Output supply required by the circuit on the positive rail; $-P_{OUT}$ = Converter Output supply required by the circuit on the negative rail; and Efficiency = Eff. / 100%. This converter has a power output rating of 22.60W for the +15V output, so the input power is calculated to be:

$$P_{IN} = \frac{+P_{OUT}}{\text{Eff}} = \frac{22.68W}{0.90} = 25.20W$$

The power consumed by the converter is calculated to be:

$$P_{IN} - (+P_{OUT}) = 25.20 - 22.68 = 2.52W$$

Therefore, for the sake of the power analysis table, the following current is shown for the +15V converter:

$$I = \frac{P}{V} = \frac{2.52W}{12V} = 0.21A$$

This implies that the converter will consume 2.52W or 0.21A from the battery to supply 15V or 22.68W required on the positive rail. Likewise, the negative rail converter has a power output rating of 8.24W for the -15V output, so the input power is calculated to be:

$$P_{IN} = \frac{-P_{OUT}}{\text{Eff}} = \frac{8.24W}{0.90} = 9.15W$$

The power consumed by the converter is calculated to be:

$$P_{IN} - (-P_{OUT}) = 13.51W - 8.24W = 0.92W$$

Therefore, for the sake of the power analysis table, the following current is shown for the -15V converter:

$$I = \frac{P}{V} = \frac{0.92W}{12V} = 0.08A$$

This means that the converter will consume 0.92 W or 0.08A from the battery to supply the -15V or 8.244 W required on the negative rail.

D. THE OSCILLATOR

After modeling different types of oscillators in LT Spice, the Wien Bridge Oscillator was the preferred choice. It was difficult to achieve and maintain oscillation after the circuit was built, and component values had to be carefully optimized. Even after oscillation was achieved, it was difficult to maintain a stable amplitude. To stabilize the operation of the oscillator, a gain stabilization circuit was introduced into the loop as this was a critical factor in achieving a stable circuit. The circuit feeds back the half-wave rectified oscillator output to stabilize the amplitude of the oscillator.

Effect of Op-Amp on the Oscillator

An op-amp has many poles that are compensated so that they are dominated by a single-pole over a specified bandwidth. This means that the loop gain of the oscillator, Aβ, is frequency-dependent through the op-amp gain, A. Equation 1 shows the dependence with the maximum open-loop gain, the dominant pole frequency ωa, and the signal frequency (ω). The frequency dependence of the op-amp gain and phase is shown in Figure 7. The op-amp closed-loop gain, $A_{CL} = \frac{1}{\beta}$ is constant with frequency such that it affects the op-amp open-loop gain at ω_{3dB} [13]. This is because of the closed-loop gain A_{CL} does not contain any poles or zeros.

At the cut-off frequency, fc, the amplitude of the signal is attenuated by 3 dB with a phase shift of 45° and the gain rolls off at -20 dB/decade until the other poles and zeros come into play [5]. The higher the closed-loop gain, A_{CL}, the earlier it intercepts the op-amp gain

$$A = \frac{a}{1+j\frac{\omega}{\omega_a}} \qquad (1)$$

It is important to also note that the phase shift contributed by the op-amp can lower the oscillation frequency and thus affects the performance of the oscillator, and the oscillator can cease to oscillate because of a decrease in closed-loop gain A_{CL} could potentially cause Aβ < 1.

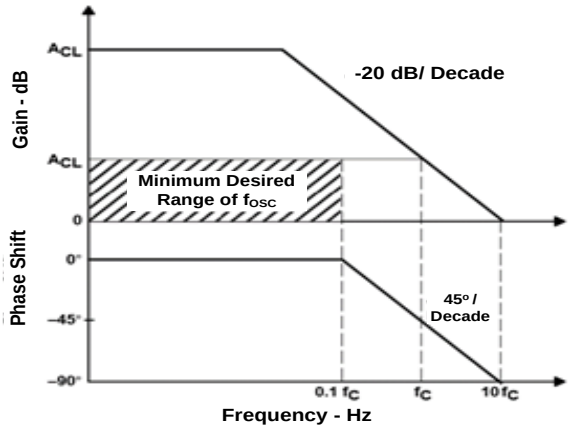

Figure 7. Op-Amp Frequency Response [5].

Oscillator Operation

Figure 8(a) shows the basic negative feedback amplifier block diagram with a positive feedback loop added. The gain of the negative feedback path is combined into a single gain term, which represents the closed-loop gain whenever positive and negative feedback is used. Figure 8(b) shows the reduced portion of Figure 8(a) with the positive feedback network represented by β =β_2.

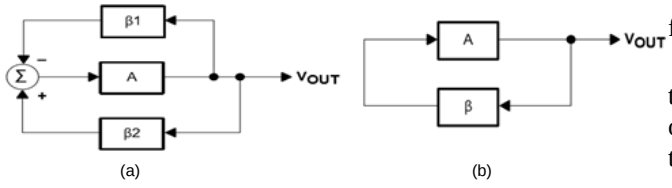

Figure 8. (a) Positive and Negative Feedback loops; (b) Simplified feedback loop.

The general form of an op-amp with positive and negative feedback is shown in Figure 9(a). To analyze the circuit, the positive feedback loop is broken at the output marked X without altering the gain A of the circuit. A test signal (V_TEST) is then applied to the broken loop and the output voltage (V_OUT) is measured with the equivalent circuit in Figure 9(b).

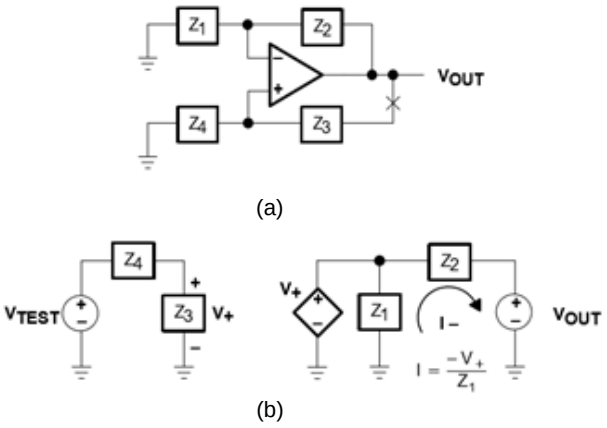

Figure 9. Positive and Negative Feedback Amplifier.

The Voltage at V_+ is calculated using equation 2.

This serves as an input signal to the noninverting input of the amplifier, which then produces a voltage output signal V_{OUT} yielding equation 3. Substituting equation 2 for V_+ in equation 3, produces equation 4, which is used to calculate the transfer function. This is true for a large op-amp open-loop gain with oscillation frequency less than $0.1\omega_{3dB}$. The Wien bridge oscillator uses both the negative feedback (β_1) and positive feedback (β_2) to achieve constant oscillation

$$V_+ = V_{TEST}\left(\frac{Z_3}{Z_3+Z_4}\right) \quad (2)$$

$$V_{OUT} = V_+\left(\frac{Z_1+Z_2}{Z_1}\right) \quad (3)$$

$$\frac{V_{OUT}}{V_{TEST}} = \left(\frac{Z_1+Z_2}{Z_1}\right)\left(\frac{Z_3}{Z_3+Z_4}\right) \quad (4)$$

Figure 10 shows the basic Wien bridge circuit configuration. On the positive side, this circuit has only a few components and good frequency stability but, the output amplitude for this circuit is at the rails, which saturates the op-amp output transistors and causes high output distortion [13]. Minimizing this distortion is more of a challenge than getting the circuit to oscillate. Fortunately, there are a few ways to minimize this effect and will be covered shortly.

The transfer function of the circuit in Figure 10 can be determined using the analysis from Figure 9. It can be seen that $Z_1 = R_G$, $Z_2 = R_F$, $Z_3 = (R_1 + 1/sC1)$ and $Z_4 = (R_2 // 1/sC2)$. The loop is then broken between the output and the component Z_1, and hence by applying V_{TEST} to Z_1, and then calculating the output Vout. The positive feedback voltage, V_+ is calculated from equations 5 through 7. Equation 5 is a simple voltage divider at the noninverting input of the op-amp. To get equation 6, each term is multiplied by ($R_2 C_2 s + 1$) and then divided by R_2 as shown.

$$V+ = V_{TEST}\left(\frac{Z_2}{Z_3 + Z_4}\right) = \left[\frac{\left(\frac{R_2}{R_2 C_2 s + 1}\right)}{\left(\frac{R_2}{R_2 C_2 s + 1}\right) + \left(R_1 + \frac{1}{C_1 s}\right)}\right] \quad (5)$$

$$\frac{V+}{V_{TEST}} = \frac{1}{1 + R_1 C_2 s + \frac{R_1}{R_2} + \frac{1}{R_2 C_1 s} + \frac{C2}{C1}} \quad (6)$$

Hence substituting s = j ω_0 and ω_0 is the oscillation frequency, $\omega_1 = \frac{1}{R_1 C_2}$ and $\omega_2 = \frac{1}{R_2 C_1}$ And this gives

$$\frac{V_+}{V_{TEST}} = \frac{1}{1 + \frac{R_1}{R_2} + \frac{C2}{C1} + j\left(\frac{\omega_0}{\omega_1} - \frac{\omega_2}{\omega_0}\right)} = \frac{1}{3 + j\left(\frac{\omega_0}{\omega_1} - \frac{\omega_2}{\omega_0}\right)} = \frac{1}{3} \quad (7)$$

It is now apparent that some relationship exists within the parameters given in equation (4). Both ω_1 *and* ω_2 represent capacitors at zero and at the pole respectively, this capacitors, each contribute a 90° phase shift for the required 180° phase shift needed for oscillation to occur at ω_0 [5]. Note that it is necessary that $C_1 = C_2$ and $R_1 = R_2$ in order to achieve this. When ω_1 *and* ω_2 are set to be the same as ω_0, this will cancel the frequency terms. and therefore, any change in the amplitude with frequency will be removed since the pole and the zero negate one another resulting in an overall feedback factor of $\beta = \frac{1}{3}$ [13].

This requires that the gain A, of the negative feedback portion of the circuit, must be set in such a way that $|A\beta| = 1$, since $\beta = \frac{1}{3}$ this implies that, A = 3. The gain value is achieved by setting $R_F = 2R_G$.

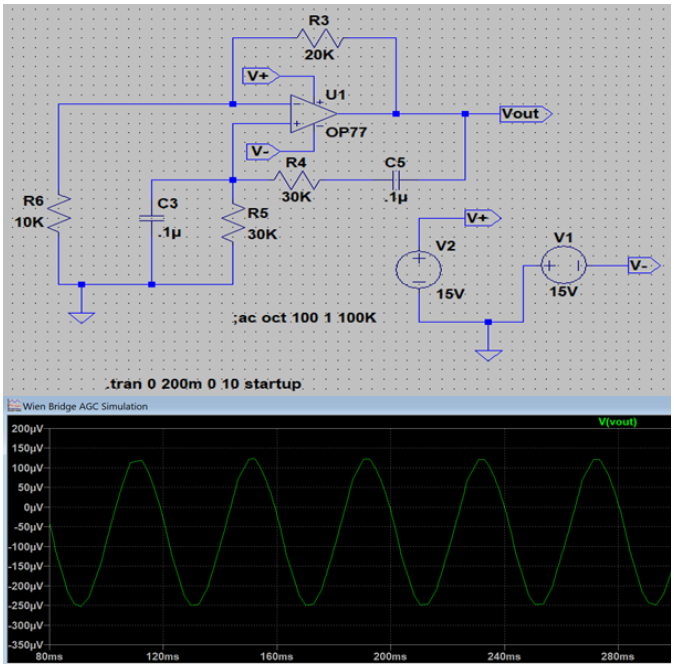

Figure 10. The Basic Wien-Bridge Oscillator Circuit and the corresponding waveform.

The component values for the circuit above are selected to provide an oscillation frequency of $\omega_0 = 2\pi f_0$, where $f_0 = \frac{1}{2\pi RC} = 25$ Hz. The circuit Oscillated at 24.8 Hz due to varying component values with more than 3% distortion well over the allowable 0.2% distortion. This is due to the extensive clipping of the output signal at both the supply rail. Increasing the feedback resistor R_f causes saturation to increase resulting in increased distortion. Using a ±1% R_f decreasing R_f by less than 1% causes the oscillator to cease [13].

Automatic Gain Control (AGC)

The use of an automatic gain control is necessary to tame the amplifier distortion. Figure 11 shows the Wien bridge oscillator with an AGC. The AGC is used to stabilize the magnitude of the sine wave output to an optimum gain level. The JFET serves as the AGC element providing excellent control due to its wide range of drain-to-source resistance (R_{DS}) controlled by the gate voltage [13]. When power is applied, the gate voltage of the JFET is zero and thus turns on with a low drain-to-source resistance (R_{DS}). This places $RG_2 + R_S + R_{DS}$ in parallel with RG_1, raising the gain over 3.0, and oscillation begins [13]. As the output voltage gradually build-up, the negative swing turns the diode on and the sample is stored on C_1, providing a dc potential to the gate of Q1. Resistor R_1 limits the current and establishes the time constant for charging C_1 (which should be much greater than f_{osc}). When the output voltage drifts high,

R_{DS} increases, lowering the gain below 3 ($1+R_f/RG_1$) [13]. The output stabilizes when the gain reaches 3. The distortion of the AGC is less than 0.2%.

With the given component values, the oscillator output voltage is at 9.69 VRMS which is then fed into the Power Amplifier noninverting input through a voltage divider. The voltage divider is made of a 2KΩ and an 84Ω resistors to provide a voltage input of 0.048V to the power amplifier.

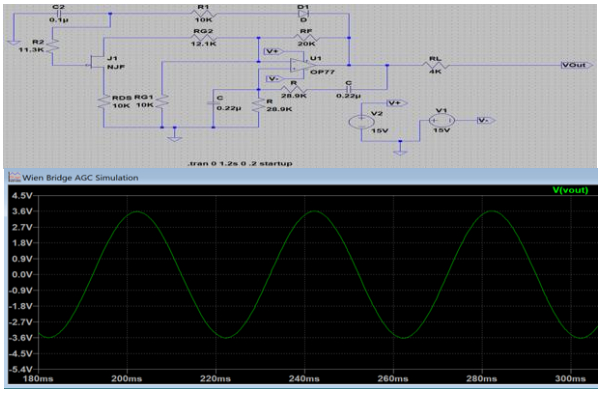

Figure 11. Wien Bridge Oscillator with Automatic Gain Control (AGC) and Wien-Bridge Oscillator Circuit Waveform.

E. AC and DC Power Supply

The power amplifier consists of an OPA549S operational amplifier that is capable of providing 10A and 8A of continuous current [13]. This amplifier provides sufficient current to power the drive coil used for this application. The OPA549 is set to operate from a dual ±15V power supply. Because the power amplifier needs current feedback to eliminate variation in the magnetic field amplitude as the coil warms up, an INA103KP instrumentation amplifier that provided current feedback to the power amplifier was the device of choice. However, it was difficult to control the gain of the amplifier and as such, there was a huge distortion in the power amplifier output and a very high gain that was sensitive to any variation in resistor values. The current supply was too high as well and the current could not be controlled, therefore, the coil was getting warmer, this is needed with highly distorted current from the detection coil. The 16 pin INA103KP was replaced with an 8 pin INA217 instrumentation amplifier. The circuit immediately responded as expected and the current was stabilized as the coil warms up to 40 degrees Celsius. This is achieved by feeding the output of the power amplifier to the input of the INA217 noninverting input and the output of the INA217 then serves as the feedback for the OMP549S Power Amplifier through a 4KΩ and a 1KΩ precision resistors as shown in Figure 12. The amplifier is set to supply 0.580A power to the AC coil set through the 0.02Ω current sense resistor as seen. It is also important to note that the OPA549 power amplifier input voltage range is limited at (V-) -0.5 V to (V+) +0.5 V and this means that input signal greater than the given range may result in permanent damage to the system or unreliable results. With the current setting, the power amplifier input voltage is trimmed down to 40mV using the voltage divider configuration shown. A 9.6V is fed from the oscillator through a 20KΩ resistor and a pull-down resistor of 84 Ω provides a regulated input voltage to the power amplifier.

The amplifier input voltage is given by V4 = $\frac{9.6V(0.084)}{0.084+20000}$ = 0.040Mv, Where V4 is the voltage at the Amplifier noninverting input pin 4.

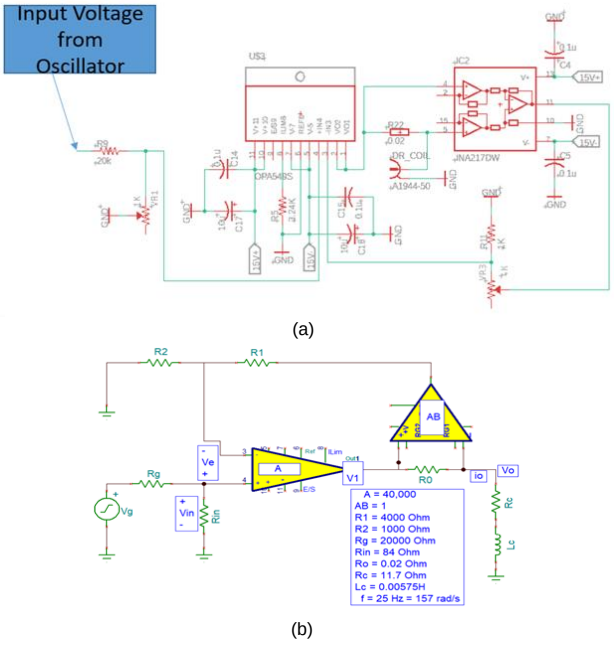

Figure 12. *(a) Power Amplifier Circuit with Current Monitor; (b)* Power *Amplifier diagram.*

The Loop transmission, T, from the amplifier in the block diagram in Figure 12(b) is:

$$V_{in} = Vg\left(\frac{R_{in}}{R_{in}+R_g}\right) = V_e^+$$

$$V_f = i_o R_0 A_B$$

$$V_e^- = V_f\left(\frac{R_2}{R_1+R_2}\right)$$

$$V_1 = A(V_e) = A(V_e^+ - V_e^-)$$

$$V_o = V_1\left(\frac{R_c + Jwl_c}{R_o + R_c + Jwl_c}\right)$$

$$\frac{V_e}{i_o} = \frac{A}{R_o + R_c + Jwl_c}$$

$$A_{OL} = \frac{i_o}{V_e} = \frac{A}{R_o + R_c + Jwl_c}$$

$$B = \frac{V_e}{i_o} = \frac{R_o R_2 A_B}{R_1 + R_2}$$

$$T = A_{oL}B = \left(\frac{A}{R_o + R_c + Jwl_c}\right)\left(\frac{R_o R_2 A_B}{R_1 + R_2}\right)$$

$$Therefore, \quad |T| = \frac{A}{\sqrt{(R_o + R_c)^2 + (wl_c)^2}}\left(\frac{R_o R_2 A_B}{R_1 + R_2}\right)$$

Note: ω = 2π X 25 Hz = 157rad/s and all other values are identified in the circuit in Figure 12. For this circuit, the loop transmission is 1361. The gain with feedback circuit, B, is the inverse of the feedback circuit which is given by:

$$A_f = \frac{1}{B} = \frac{(R_1 + R_2)}{R_o R_2 A_B} \gg 1$$

For the values given in Figure 12, the feedback stabilized gain is 2.5. The DC power amplifier is a replica of the AC Power amplifier with a few changes in the input signal. The input signal of the power amplifier is supplied through a precision adjustable shunt voltage reference device (LMV431). The amplifier feedback is set to provide a 1.37V, 0.8A power supply to the bias coil through an adjustable voltage reference.

F. 4.6 Low Noise Transimpedance Amplifier

The preamplifier circuit selected for this application is the INA217 device with a low-noise, low-distortion, monolithic instrumentation amplifier [6], [15]. The induced current on the detection and cancellation coil from the AC drive coils feeds the input signal of the transimpedance amplifier through RG1 and RG2 as shown in the circuit below. When the detection current is feed through the gain resistor, this set upturns the Instrumentation Amplifier into a transimpedance amplifier and has a transimpedance which equals twice the value of the feedback resistor Rf (5K). The response of the preamp provided lower noise than the commercial preamplifier (DLPCA-200) designed by Femto during testing at the Y-12 facility.

The instrumentation amplifier (IA) circuit shown in Figure 13 has a highly accurate current-to-voltage conversion which has a transimpedance dependent only on the feedback resistance (R_f) value (5KΩ in this case) of the IA input stage [14], [15]. If A1 and A2 inverting-input bias currents are neglected, the detection coil current flows in the two R_f feedback (5KΩ) resistors (Texas Instrument, 2002). The V_{IN+} pin (3), V_{IN-} pin (2), and REF pin (5) are all connected to the ground, such that RG_1 pin (1) and RG_2 pin (8) now becomes the IA input. Since V_{IN+} and V_{IN-} are connected to the ground, the A3 difference amplifier will only see R_f * I_{coil} and $-R_f$ * I_{coil} voltages at its inputs [6]. Therefore, the IA now output voltage will be:

$$V_o = 2 * R_f * I_{coil} \qquad (8)$$

I_{coil} is the current induced by the detection coil. The output voltage V_o feeds into the noninverting input V_{IN+} pin (3), of the second stage IA. The second stage amplifier gain is set using the one resistor on RG1 pin (1) and RG2 pin (8) which determines the overall gain of the IA. There seems to be an issue of clipping with the second stage amplifier connected and the remedy to fix the clipping was to reduce the gain of the transimpedance amplifier, this was achieved only by completely removing the second stage of the amplifier.

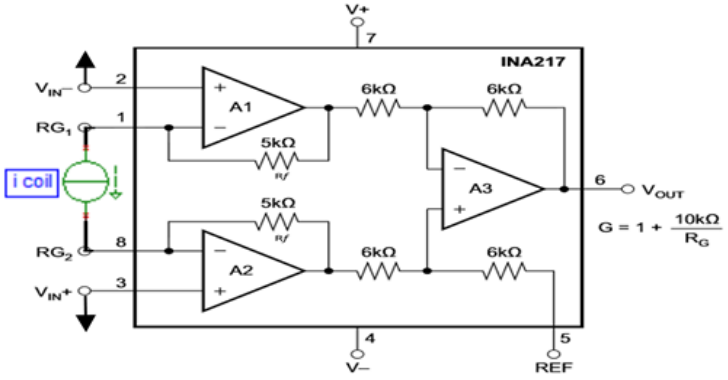

Figure 13. Instrumentation Amplifier Block Diagram [14].

G. 4.7 AC Drive Coil

The AC excitation coil, as seen in Figure 14, is fabricated on a 12 inches Pyrex tubing: with an outside diameter OD = 0.411" and an inside diameter ID =0.34". The wall thickness of this tube is the difference between the OD and ID divided by two. A 24 gauge copper wire is wrapped around the tube forming a 6 layer solenoid as shown in figure 13. The total outside diameter of the coil is 0.66" with a total length of 9.63". Each layer has a total of 456 turns and a total wire length of 953.5 per layer for a total wire length of 2738 inches for the entire 10 layers. The Coil resistance of 11.7 Ohms and inductance of 5.7mH. This yields an RL cut frequency fc of R/2πL = 327Hz. The typical coil current is 1.4 $A_{rms.}$ However, the coil will only be feed 0.586A through a 50Ohm BNC connector. Figure 16 shows the specifications used in the fabrication of the Drive coil.

(a) (b)

Figure 14. *(a) AC* Drive Coil *Fig. 15(b) AC Drive coil with shrink wrap protection.*

The detection coils are located approximately in the center of the AC drive coil with the cancellation coils alongside the detection coil in series. The 0.98 Ω series impedance of both coils will match the 50 Ω input impedance of the current preamplifier. If more turns of wire are increased, the sensitivity of the sensor increases

and this will, in turn, decrease the frequency response which is bounded at 10KHz as seen in fig 3b.

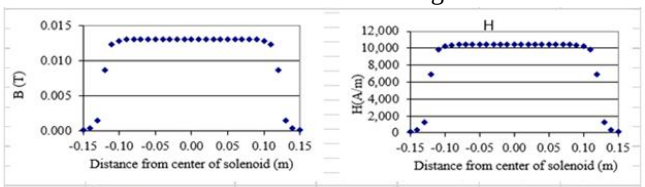

24 gauge					
Dia of Spindle	0.375 in				
Thickness ins	0.0005 in				
Thickness of tape	0.001 in				
Dia wire	0.0201 in				
Dia wire+2x ins + ta	0.0221 in				
Dia wire+2x ins	0.0211 in				
length of wire	7312.7 in		185.7429 m		
Resistance of wire per length			0.084198 Ohms/m		
Calc coil res			15.63911 Ohms		
Meas coil resistance			11.1 Ohms		
coil	length of coil	rad of coil	ngth of wrap		Turns
1	9.63	0.199	953.5	in	456
2	9.63	0.221	1059.6	in	456
3	9.63	0.243	1165.7	in	456
4	9.63	0.265	1271.8	in	456
5	9.63	0.287	1378.0	in	456
6	9.63	0.309	1484.1	in	456
wire length			7312.7	in	2738
Average	9.630	0.254		in	
Average	0.2446	0.0064		m	
Maximum		0.3201			

Figure 15. Drive *coil Specifications.*

Figure 15 shows the magnetic field strength in B (T) and H(A/m) respectively from the center of the solenoid. Figure 16 shows the number of layers wound around the Pyrex tubing glass tube covering a length of 9.63 inches for a total of 456 turns in each of the 6 layers. Overall, a total of 7312.7 inches (185.7429 m) of 24 gauge was used for a total calculated resistance of 15.63933 Ohms, (11.1 Ohms Measured) was achieved. The coil is connected through a 50 Ohm BNC connector to be connected to the circuit.

The Frequency response of the AC drive coil, detection coil, and the cancellation coil is shown in Figure 16. The AC drive coil has an input impedance of 0.02 Ohm from the amplifier and has an LR cut frequency of 584 Hz. The cable has an internal capacitance of 3.30E-11F and LC cut the frequency of 4.22E05Hz. The detection coil and cancellation coil both have an amplifier input/output impedance of 60Hz with a total cable capacitance of 3.30E10F. The LR cut frequency for the detection and cancellation coil is 6.56E05Hz.

Frequency Response of AC Drive Coil and the Detection/Cancellation Coil Set

	10" long Drive Coil	Combined Sense Coil Set Detection	Cancellation	
Wire Gauge	24	30	30	
Mean radius coil, a	0.2538	0.133	0.140	in
OD of coil	0.6402	0.283	0.308	in
Wire diameter	0.0201	0.0100	0.0100	in
Insulation Thickness x2	0.0009	0.0025	0.0025	in
Tape Thickness		0.004	0.002	in
Wire resistance/length	103.2	103.2	103.2	Ohm / 1000'
Wire resistance/length	0.0086	0.0086	0.0086	Ohm / inch
Individual Coil Resistance	15.64	3.252	3.486	Ω
Coil Height, b	9.6300	5.6563	2.8959	In
Mean Circumference	1.653106054	0.837	0.877	in
turns (one coil all layers)	2738	452	462	
Length of Wire	7313	378	405	in
Wire cross sectional area				in^2
Coil cross sectional area				in^2
Coil cross sectional width, c	0.1326	0.013	0.025	in
Total coil diameter	0.3201	0.279	0.304	in
Coil spool diameter	0.375	0.250	0.250	in
Inductance (Wheeler) p62 Terman	0.0043	0.000056	0.000123	H
Amplifier Output/Input Impedance	0.2	60		Ω
LR Cut Frequency (1 coil)	584	59488		Hz
LR Cut Frequency (2 equal coils)				Hz
Layers of wire in coil	6	1	2	
Cable Capacitance	3.30E-11	3.30E-10		F
LC Cut Frequency	4.22E+05	6.56E+05		Hz
Series shunt resistance	0	0	0	Ω

Resistance		
Calculated	15.6 W	6.7 Ω
Measured	11.7 W	7.2 Ω
Inductance		
Calculated	0.0043 H	0.00012 H
Measured	0.0058 H	0.00019 H

Figure 16. Frequency response for the AC Drive Coil, Detection Coil and Cancellation coil.

H. DC Bias Coil

The DC bias coil is fabricated on a 12 inches Pyrex tube with an OD = 0.98" and ID = 0.87". The wall thickness of this tube is the difference between the OD and ID divided by two. The Bias coil provides a DC magnetic field gradient to separate peaks from the detection coil in time. It provides a field similar to a Maxwell coil but uses a solenoid. The maximum coil OD is 1.668" at either end of the coil. The typical coil current is 0.8 A_{dc}. The coil is wound in the section of 20 equal divisions with varying density in each of the sections using an 18-gauge copper wire. The 20 equal sections on the coil are split in half, the second half is wound with the same density variation as the first, but the direction of the winding is reversed for the next 10 sections. This process is repeated for each of the 10 layers of the drive coils. Because the sections in each layer have varying density, where the second half of the tube is a mirror of the first ten sections. The coil has an overall length of 9.625 inches on the tube with 1.19 inches of tubing left on both sides of the coil. The 10-layer coil wound from 18 gauge wire with 128 turns per layer or 1280 turns total as shown in Figure 17.

18 gauge wire version used in first prototype					
	Dia of Spindle	0.75	in		
	Dia wire	0.041	in		
	Thickness of tape	0.002	in		
	Dia wire + 1 layer tape	0.043	in		
	length of wire	4809.7	in	122.1671	m
	Resistance of wire per length			0.02095	Ohms/m for 18 gauge wire
	Calc coil res			2.559401	Ohms
	Meas coil res			0.9	Ohms

coil	length of coil	rad of coil	length of wrap		Half Coil Turns
1	9.63	0.404	325.2	in	64
2	9.63	0.447	359.8	in	64
3	9.63	0.490	394.4	in	64
4	9.63	0.533	429.1	in	64
5	9.63	0.576	463.7	in	64
6	9.63	0.619	498.3	in	64
7	9.63	0.662	532.9	in	64
8	9.63	0.705	567.5	in	64
9	9.63	0.748	602.1	in	64
10	9.63	0.791	636.7	in	64
wire length			4809.7	in	640
Avg Rad (in)	9.625	0.598		in	
Avg Rad (m)	0.2445	0.0152		m	
Max. OD (in)		1.668			

Figure 17. The density of the DC bias Coil in each of 20 equal sections.

I. Detection and Cancellation Coil

The AC detection/cancellation coil is fabricated on a 12 inches Pyrex tubing: with an outside diameter, OD = 0.276 Inch and an inside diameter ID =0.197 Inch. The detection coil picks up the Faraday voltage created by fluctuations in the magnetic flux from the AC drive coil. These coils serve the same functions as the "exciting" and "response" coils in the wireless radiation sensor described by Du et al. [16]. In the configuration reported in [17], the detection and cancellation coils are wound on the same mandrel Pyrex tubing. The detection coil is designed such that one-layer 30-gauge copper wire is wound around the Pyrex tube covering 5.66 inches in length with a total of 452 turns. The overall outside diameter OD of the detection coil is 0.252 inch with an expected coil resistance of 0.715 Ω as seen in Figure 18.

Figure 18. Detection and Cancellation Coil.

The cancellation coil is wrapped on the same Pyrex tube as the detection coil with a length of 2.90 inches, 213 turns in each of the two layers making a total of 426 turns. The cancellation coil is separated from the detection coil by a gap of 0.20 inches. The coil also has an expected total resistance of 0.771 Ω. The overall length of the detection and cancellation coil is the sum of the detection coil length, cancellation coil length, and the gap between each coil which totals 8.76 inches. See Figure 19 for the detailed fabrication process.

Length and number of turns for Detection / Cancellation Coil						
			dimension (in)			
100.2377	3 Phases	4 Phases				
As-built	Prototype	Prototype	First try			
	7.874016	7.874016	7.874016	length of solenoid's iso-field		
	9.63	9.63	9.63	length of solenoid		
	1.75	1.75	1.75	length of gradient field in solenoid		
	8.749508	8.749508	8.749508	expected length of detection and cancelation coil if cancellatic		
	0.6	0.6	0.75	needed length for fitting		
	10.1875	10.1875	10.1875	length of ac coil with shrink		
	12	12	12	length of detection tube		
	0.965	0.965	0.5	Bias of spare toward detection coil		
	0.591063	0.591063	0.15625	spare for electrical connections on detection coil side		
	0.021438	0.021438	0.15625	spare for electrical connections on cancellation coil side		
	0.21875	0.21875	0.28125	shrink on detection side of ac coil including wrap on mandrel		
	0.34375	0.34375		shrink on cancellation side of ac coil including wrap on mandre		
					Qty	length (in)
	1.689	2.375	2.375	total length of phases	3	0.563
	4	3.28125	3.28125	total length of gaps between phases	2	1.2
	5.689	5.65625	5.65625	needed length for four phases	2	0.8
5.689	5.689	5.65625	5.65625	length of detection coil	4	0.59375
	251.7257	250.2765	250.2765	turns needed in detection coil	5	0.65625
	8	8	6	extra turns for cancellation coil		
big	129.8628	129.1383	128.1383	turns needed in cancellation coil x2		
2.957	2.9349	2.918525	2.895925	length of cancellation coil		
	8.6239	8.574775	8.552175	total length of cancellation coil and detection coil		
0.118	0.125608	0.174733	0.197333	gap between detection and cancellation coil		
	8.749508	8.749508	8.749508	Total length of detection coil, cancellation coil, and gap		
2.285	2.285305	2.285305	2.062992	start of detection coil from tube end		
0.966	0.965188	0.965188	1.1875	start of cancellation coil from other end of tube		
12.015	12	12	12	check on total length of tube		

Figure 19. Length and Number of Turns for Detection/Cancellation coil.

J. Air Sampling Pump

The double-headed KNF micro diaphragm gas sampling pump features a head connection for the two pump heads that are integrated into the housing operates with an extremely low level of noise [7]. The pump diaphragm is coated with PTFE for chemical resistance and is used in conjunction with the flow meter to sample the amount of gas pumped through the TRM. The 12V Brushless DC motor pump draws its power directly from the battery power supply.

K. Display /Microprocessor

For better sampling and processing, a LabJack T7 with a resolution of 16-bit to 24-bit analog inputs, and an option to use USB, Ethernet, or WiFi, also have numerous built-in firmware features is a good candidate accomplish nearly any data acquisition necessary in this work. The LabJack will be used for acquiring signals from the sensor and will serve that sensor data out through any of its 3 communication interfaces to the Raspberry Pie microprocessor. The Raspberry Pie 3 model B has a 64-bit quad-core processor running at 1.4GHz, dual-band 2.4GHz and 5GHz wireless LAN, Bluetooth 4.2/BLE, faster Ethernet, and PoE capability via a separate PoE HAT. The Microprocessor can be programmed using python to perform averaging output to be displayed on a 3.5 inches HDMI LCD, 480x320.

5. RESULTS AND DISCUSSION

There has been a significant amount of work done on sensors that operate on the principle of the magnetic field.

As mentioned in the introduction, the analysis system for the magnetoelastic radiation sensor is very similar to that used in [4]. This system was refined several times during the development of ChIMES technology but is still considered immature [4]. Much of the work reported here was concerned with reducing the size of the entire sensor design from benchtop size used in [4] to a handheld device.

The ChIMES design is unique and made up of few components which allow it to be light, portable and interchangeable sensor heads. The system is powered by a 12 volts battery which supplies 15 volts power to all the active components through a dc to dc boost converter.

The oscillator which is designed base on the Wein bridge principle with automatic gain control for stability and low distortion comprises a general-purpose amplifier and a few resistors, capacitors, transistors and a diode. This oscillator performed well as expected and generated a 9.63 volts rms at 25Hz as tuned.

Signal generated by the oscillator is feed into the ac power amplifier through a voltage divider so supply the recommended signal to the power amplifier. The op-amp is designed with a current limit of 2 Amps and provides the coil set with a variable current up to 10 Amps, or 8 Amps continuous. The design of the power amplifier allows it to monitor the current draw of the AC drive coil to avoid drift due to temperature change in the coil set through a current monitor.

The dc power supply is designed similarly as the ac power amplifier. However, the input signal of the dc power supplies is a dc voltage through a voltage reference to ensure stable supply under different conditions. A voltage reference was considered to provide the signal, but since the amplifier itself can be designed to general a reference supply just like the typical voltage reference, this concept seems better to reduce the number of components on the sensor electronics. An important point to note is the use of an OPA548 in place of OPA549 for the dc bias coil. This is because the OPA 548 is suitable for devices that need less than 1 Amp and has a lesser number of pins. And this makes it a good choice to use on a PCB as well as the dc bias coil which is only required to run on 0.8 Amps rms. The current limit pin of the amplifier is connected to the ground through a resistor, the resistor value selected determines the current value and the voltage supply that will be feedback into the supply signal of the amplifier.

The Power supply that drives the AC Drive coil seen in Figure 20 (purple) has a 7.4 VRMS which powers the AC drive coil through a current sense resistor at 0.8A. The magnetic field produced by the coil is induced on the Detection Coil which is seen in yellow and consequently canceled by the Cancellation coil results in net voltage output of 0. The spikes seen is the result of the induced magnetic field induced on the amorphous wire that could not be canceled by the cancellation coil. The height of the spike (amount of current on the amorphous wire) can be analyzed by a computer program to determine the presence of an analyte in the sensor head (target response material + amorphous = sensor head). Because the presence of an analyte on the sensor head will cause the sensor to respond by swelling and thereby imposing stress on the amorphous wire, the response of the amorphous wire embedded in the sensor will be relatively different, and therefore, the spike output will be different from a non-stressed sensor.

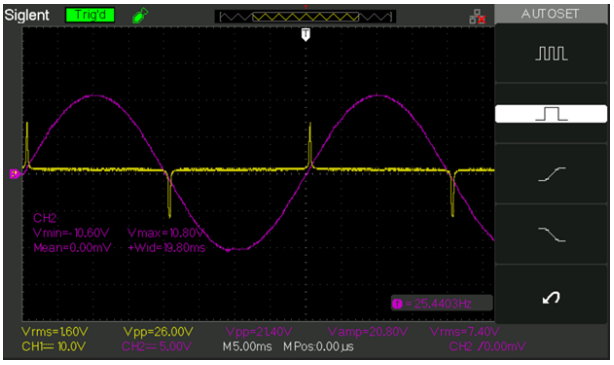

Figure 20. Sensor Signal Output.

The circuit board was designed on a two-layer board measuring 5.203 IN X 3.307 IN as shown in Figure 21.

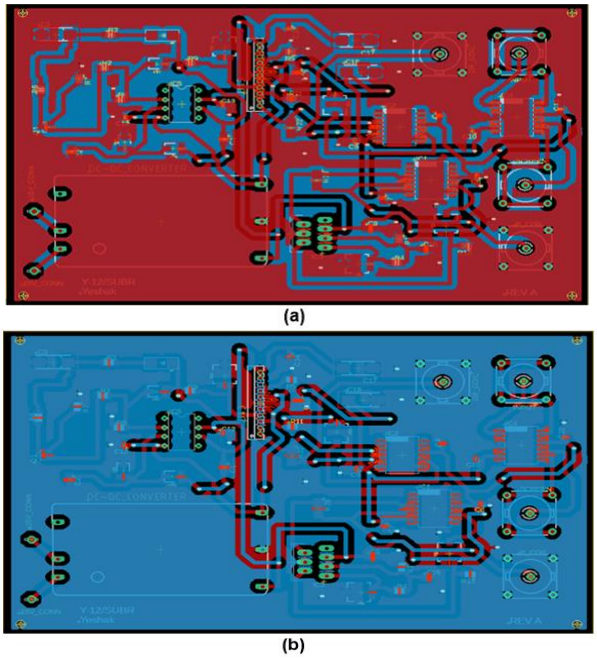

Figure 21. (a) Top Layer of Printed Circuit Board; (b) Bottom Layer of Printed Circuit Board.

6. CONCLUSION AND FUTURE WORK

Because much of the work reported here was concerned with reducing the size of the entire sensor design from benchtop size in [4] to a handheld device. This work presents the design, operational principles and applications of magnetoelastic sensors. ChIMES operates on principles of Magnetoelastic sensors which are amorphous ferromagnetic ribbons that exhibit a magneto-mechanical resonance when excited by a time-varying magnetic field. Magnetoelastic sensors have successfully been used to measure stress, pressure, liquid viscosity and density, fluid flow velocity, elasticity, and temperature monitoring. ChIMES is aimed at measuring Chemical sensors head based on the magnetoelastic sensor platform fabricated by combining the magnetoelastic sensors with mass changing, chemically responsive layers.

The design of the Oscillator is a success providing a minimal distortion at an output of 25Hz. Although the oscillator output was far larger than desired providing an output close to the rail, the output is then dropped to the desired range through the use of a voltage divider constructed from a precision resistor. The Power amplifier performed as expected, providing an output of nearly 26V from an input of 80mV. The power amplifier design which provides an adjustable current between 0.3 and 0.9A through a 0.02Ohm current sense resistor to the AC drive coil performed seamlessly. The entire circuitry performed well, warming the AC drive coil to the desired temperature of 40 degrees Celsius in less than two minutes and the coil temperature became stable and ready for sampling.

Future work will be performed to provide a fully built sensor with the microprocessor and screen display required to show results of sampled analytes.

ACKNOWLEDGMENT

The authors would like to thank the Research on science and engineering of signatures (ROSES), the Department of Electrical Engineering, and the Department of Mechanical Engineering of Southern University and A&M College, Baton Rouge, USA for the great support provided in full to finalize this work.

REFERENCES

[1] D. Atkinson, et al., "An integrating magnetic sensor based on the giant magneto-impedance effect," Sensors and Actuators journal, Elsevier Science publisher, vol. 81, Issues 1–3, pp. 82-85, 2000.

[2] G. Yu, et al., "Differential-type GMI magnetic sensor based on longitudinal excitation," IEEE Sens. J., vol. 11, no. 10, pp. 2273–2278, 2011.

[3] M.G. Nematov et al.," IEEE International Magnetics Conference (INTERMAG), 24-28 April 2017.

[4] N. A. Hatab et al., "Chemical Sensor Based Upon Stress-Induced Changes in the Permeability of a Magnetoelastic Wire," Anal. Chem., vol. 89, no. 13, pp. 6976–6983, 2017.

[5] W. Zhao, et al., "Feedback-type giant magneto-impedance sensor based on longitudinal excitation," J. Magn. Magn. Mater., vol. 324, no. 19, pp. 3073–3077, 2012.

[6] C. A. Grimes, et al., "Theory, instrumentation and applications of magnetoelastic resonance sensors: a review.," Sensors (Basel)., vol. 11, no. 3, pp. 2809–44, 2011.

[7] V. Lamberti, D. Mee, P. Angelo, and J. Preston, "A passive magnetoelastic radiation sensor," *Sensors (Switzerland)*, vol. 19, no. 22, 2019.

[8] Y. Honkura, "Development of amorphous wire type MI sensors for automobile use," in Journal of Magnetism and Magnetic Materials, 2002.

[9] T. Uchiyama, et al., "Biomagnetic field detection using very high sensitivity magnetoimpedance sensors for medical applications," Phys. Status Solidi Appl. Mater. Sci., 2009.

[10] Y. Jiang, et al., "Design of magnetic sensor based on the asymmetric giant magneto-impedance effect in amorphous alloys," Chinese J. Sensors Actuators, vol. 24, no. 2, pp. 175–179, 2011.

[11] C. A. Grimes *et al.*, "Wireless magnetoelastic resonance sensors: A critical review," *Sensors*, vol. 2, no. 7, pp. 294–313, 2002.

[12] "TEN 60-1223N - TRACO Power - TRC Electronics." [Online]. Available: https://www.trcelectronics.com/View/TRACO-Power/TEN 60-1223N.shtml. [Accessed: 26-Nov-2018].

[13] D. Patranabis and P. C. Sen, "A sine wave oscillator," Int. J. Electron., vol. 29, no. 5, pp. 441–447, 1970.

[14] Texas Instruments, "INA217 INA217 Low-Noise, Low-Distortion Instrumentation Amplifier Replacement for SSM2017," 2002.

[15] Ross Kulak, et al., "A multimode 76-to-81GHz automotive radar transceiver with autonomous monitoring," IEEE International Solid - State Circuits Conference - (ISSCC), pp. 158 – 160, 2018.

[16] N. Du *et al.*, "Developing a wireless sensing method for the measurement of gamma radiation dose based on the polymerization of acrylamide," *Radiat. Meas.*, vol. 47, no. 5, pp. 371–374, May 2012.

Mr. Yeshak Dabels received his B.Sc. degree in Electrical Engineering from Southern University and A&M college Baton Rouge in 2017 and later received his M.E in Electrical Engineering from Southern University and A&M College in 2018, he is the founder of the Southern University Microcontroller Club (SUBR MCC) and currently working on his MBA Data Analytics concentration at Louisiana State University Shreveport. He is also a veteran of the United States Army, currently serving in the Louisiana National Guard as an Aircraft Electrician. Mr. Yeshak Dabels is currently working at Lockheed Martin Co. on the Joint Strike Fighter (JSF) the F35 multi role fighter (Aeronautics line of business) as an Electrical Engineer. He is a member of the IEEE, NSBE National, and Lockheed Martin Professionals NSBE.

Dr. Yasser Ismail received his BS. degree in Electronics & Communications Engineering from Mansoura University - Egypt, in 1999. He received his MS in Electrical Communications from Mansoura University - Egypt, in 2002. Dr. Ismail received his MSc and PhD degrees in Computer Engineering from University of Louisiana at Lafayette - USA in 2007 and 2010 and subsequently joined Umm Al-Qura University - Kingdom of Saudi Arabia as an assistant professor. In Fall 2012, he joined University of Bahrain - Kingdom of Bahrain as a Computer Engineering Assistant Professor. In Fall 2016, Dr. Ismail Joined both Electronics & Communications Engineering Department - Mansoura University - Egypt and Zewail City of Science and Technology - University of Science and Technology - Zewail City - Egypt as an assistant professor. Dr. Ismail is currently working as an assistant professor in the Electrical Engineering Department, Southern University and A&M College - Baton Rouge - Louisiana - USA. His area of expertise is Digital Video Processing Algorithms/Architectures levels, Internet of Things (IoT), VLSI and FPGA Design (Low-Power and High-Speed Performance Embedded Systems), automotive transportation, Robotics, RFID, and Wireless and Digital Communication Systems. He has published two books, two book chapters, and more than 35 articles in related journals and conferences. Dr. Ismail served as a reviewer for several conferences and journals, including IEEE ICIP, IEEE GCCCE, IEEE ICECS, IEEE MWSCAS, IEEE ISCAS, IEEE SIPS, IJCDS, Springer, Elsevier, IEEE Transactions on VLSI, IEEE Transaction on Circuit and System for Video Technology (TCSVT), and IEEE Transactions on Image Processing. He severed in the technical committees of IEEE ISCAS 2007, IEEE ICECS 2013, MobiApps 2016, IEEE Virtual World Forum on Internet of Things (WF-IoT 2020), and IEEE MWSCAS 2018, 2019, and 2020 conferences. He was invited to serve as a lead guest editor for a special issue in mobile information systems – Hindawi publishing corporation September 2016. Dr. Ismail served as a PI and Co-PI for several funded grants from NSF and other international fund agencies. Additionally, Dr. Ismail served as a member of many Editorial Boards 2018-present.

Dr. Fred Lacy received the B.S.E.E. degree and Ph.D. degree in electrical engineering from Howard University, Washington, DC, in 1987 and 1993, respectively, and the M.S.E. degree from Johns Hopkins University, Baltimore, MD, in 1989. He was a Postdoctoral Fellow in the Bioengineering Department, University of California, San Diego, for four years, where he performed research in the area of biosensors. He was with the US Food and Drug Administration, where he performed medical device reviews. In 2002, he joined the Electrical Engineering Department, Southern University and A&M College, Baton Rouge, LA, where he is engaged in research and teaches courses in solid-state electronics, electrical and electronic circuits, and electronics-based sensors.